

Study of the 2D heaving and pitching airfoil case using the Spectral Difference method

by

Caleb Yow, Bin Zhang, Chunlei Liang

Department of Mechanical and Aerospace Engineering
George Washington University
Washington DC, 20052
Phone: (202) 994-7073
chliang@gwu.edu

3rd International Workshop on High-Order CFD Methods

Sponsored by NASA, AIAA, DLR, and Army Research Office (ARO)

January 3-4, 2015

at the 53th AIAA Aerospace Sciences Meeting, Kissimmee, Florida

1 Code description

1.1 SD Method

Using the 2D spectral difference (SD) code published in [1] and [2] to handle moving and deformable grids similar to method reported in [3], Case Study 2.3 was analyzed with a third order SD method. In the SD code, the solution points and flux points are staggered within the grid in order to achieve the higher order.

The flow field within each cell is reconstructed with a smooth representation using a tensor-product form. The discontinuity across cell interfaces is handled using a Rusanov flux (Local Lax Friedrichs method). We also implemented a p-multigrid scheme for this solver. For this abstract, all results are obtained using a single-level grid with the 3rd-order SD method.

Consider the following conservative form of the 2D unsteady conservation laws:

$$\frac{\partial \mathbf{Q}}{\partial t} + \frac{\partial F}{\partial x} + \frac{\partial G}{\partial y} = \frac{\partial \mathbf{Q}}{\partial t} + \nabla \mathbf{F}_{inv}(\mathbf{Q}) - \nabla \mathbf{F}_v(\mathbf{Q}, \nabla \mathbf{Q}) = 0 \quad (1)$$

where \mathbf{Q} is the vector of conserved variables, and F and G are the total fluxes including both inviscid and viscous flux vectors.

Consider only compressible Navier-Stokes equations, the conservative variables \mathbf{Q} and Cartesian components $f_{inv}(\mathbf{Q})$ and $g_{inv}(\mathbf{Q})$ of the inviscid flux vector $\mathbf{F}_{inv}(bfQ)$ are given by

$$\mathbf{Q} = \begin{Bmatrix} \rho \\ \rho u \\ \rho v \\ E \end{Bmatrix}, \quad f_{inv}(\mathbf{Q}) = \begin{Bmatrix} \rho u \\ \rho u^2 + p \\ \rho uv \\ u(E + p) \end{Bmatrix}, \quad g_{inv}(\mathbf{Q}) = \begin{Bmatrix} \rho v \\ \rho uv \\ \rho v^2 + p \\ v(E + p) \end{Bmatrix} \quad (2)$$

where ρ is the density, u and v are the velocity components in x and y directions, p stands for pressure and E is the total energy. The pressure is related to the total energy by

$$E = \frac{p}{\gamma - 1} + \frac{1}{2}\rho(u^2 + v^2) \quad (3)$$

with a constant ratio of specific heat γ set as 1.4 for air.

The Cartesian components $f_v(\mathbf{Q}, \nabla \mathbf{Q})$ and $g_v(\mathbf{Q}, \nabla \mathbf{Q})$ of viscous flux vector $\mathbf{F}_v(\mathbf{Q}, \nabla \mathbf{Q})$ are given by

$$f_v = \mu \begin{Bmatrix} 0 \\ 2u_x + \lambda(u_x + v_y) \\ v_x + u_y \\ u \cdot f_{v[2]} + v \cdot f_{v[3]} + \frac{C_p}{P_r} T_x \end{Bmatrix}, \quad g_v = \mu \begin{Bmatrix} 0 \\ v_x + u_y \\ 2v_y + \lambda(u_x + v_y) \\ u \cdot g_{v[2]} + v \cdot g_{v[3]} + \frac{C_p}{P_r} T_y \end{Bmatrix}$$

where μ is the dynamic viscosity, C_p is the specific heat and P_r stands for Prandtl number. T is temperature which can be derived from the perfect gas assumption. λ is set to $-2/3$ according to the Stokes hypothesis.

To achieve an efficient implementation, all quadrilateral elements in the moving and deformable physical domain (x, y, t) are transformed into a square element ($0 \leq \xi \leq 1, 0 \leq \eta \leq 1, \tau = t$) as shown in figure 1. The governing equations in the physical domain are then transferred into the computational domain, and the transformed equations are written as:

$$\frac{\partial \tilde{\mathbf{Q}}}{\partial \tau} + \frac{\partial \tilde{\mathbf{F}}}{\partial \xi} + \frac{\partial \tilde{\mathbf{G}}}{\partial \eta} = 0 \quad (4)$$

where $[\tilde{\mathbf{F}} \quad \tilde{\mathbf{G}} \quad \tilde{\mathbf{Q}}]^T = |\mathcal{J}| \mathcal{J}^{-1} [\mathbf{F} \quad \mathbf{G} \quad \mathbf{Q}]^T$. The Jacobian matrix is given by

$$\mathcal{J} = \frac{\partial(x, y, t)}{\partial(\xi, \eta, \tau)} = \begin{bmatrix} x_\xi & x_\eta & x_\tau \\ y_\xi & y_\eta & y_\tau \\ 0 & 0 & 1 \end{bmatrix}, \quad (5)$$

where $t_\xi = 0, t_\eta = 0$, and $t = \tau$.

In the standard element, two sets of points are defined, namely the solution points and the flux points, as illustrated in figure 1 (b) for a computational cell. A bilinear mapping is employed to map individual physical cells shown in Fig. 1 (a) to this standard computational cell.

In order to construct a degree $(N - 1)$ polynomial in each coordinate direction, N solution points are required. The solution points in 1D are chosen to be the Chebyshev-Gauss points. The flux points $X_{s+1/2}$ are selected as the Legendre-Gauss-quadrature points plus the two end points, 0 and 1, as suggested by following [4] and [5].

Using the solutions at N solution points, a degree $(N - 1)$ polynomial can be built using the following Lagrange basis of $h_i(X)$. Similarly, using the fluxes at $(N + 1)$ flux points, a degree N polynomial can be built for the flux using a similar Lagrange basis of $l_{i+1/2}(X)$.

The reconstructed solution for the conserved variables in the standard element is just the tensor products of the two one-dimensional polynomials. The reconstructed flux polynomials are

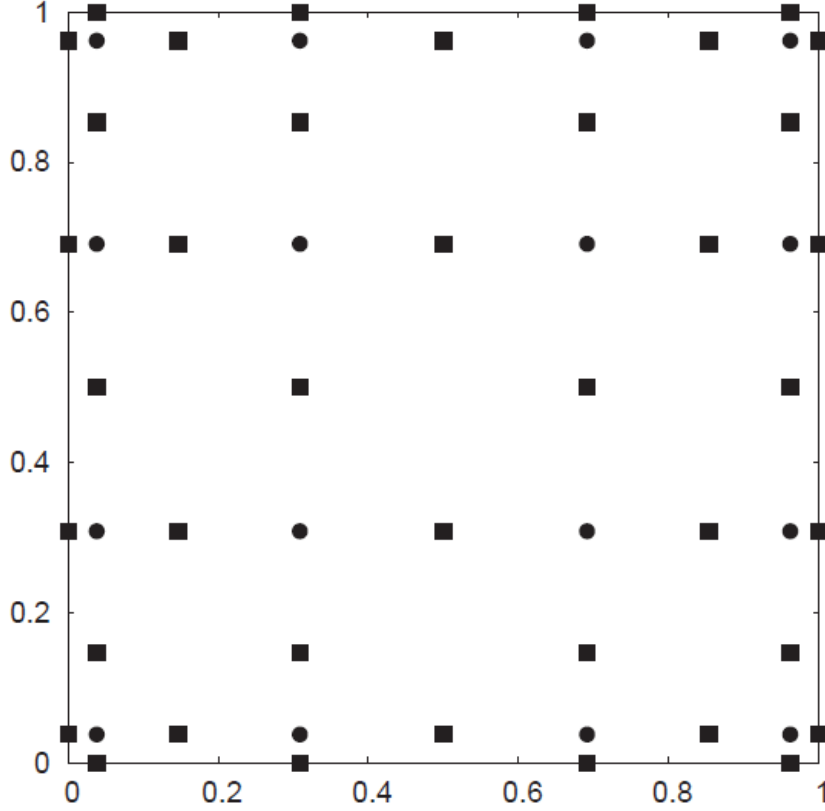


Figure 1: Physical cells and computational cell.

treated in ξ , and η directions as 1D element-wise continuous functions, but discontinuous across cell interfaces. For the inviscid flux, a Riemann solver is employed to compute a common flux at interfaces to ensure conservation and stability. For the viscous flux, an averaging procedure is used.

For dynamic grids considered here, we reformulate the Rusanov solver for the ξ direction as

$$\tilde{F}^{inv} = \frac{1}{2} \left\{ \tilde{F}_L^{inv} + \tilde{F}_R^{inv} - (|\bar{V}_n| + \bar{c}) \cdot (Q_R - Q_L) \cdot |\mathcal{J} \nabla \xi| \cdot s \right\}, \quad (6)$$

where s is the sign of $\mathbf{n} \cdot \nabla \xi$, V_n is the fluid velocity normal to edge interface and c is the speed of sound. For the η direction, it is formulated similarly.

In addition, we must consider geometric conservation law for deforming grid cells:

$$\frac{\partial |\mathcal{J}|}{\partial \tau} + \frac{\partial (|\mathcal{J}| \xi_t)}{\partial \xi} + \frac{\partial (|\mathcal{J}| \eta_t)}{\partial \eta} = 0 \quad (7)$$

The final compact form after taking into account of the geometric conservation law is given by

$$\frac{\partial Q}{\partial \tau} = \frac{1}{|\mathcal{J}|} \left\{ Q \left[\frac{\partial (|\mathcal{J}| \xi_t)}{\partial \xi} + \frac{\partial (|\mathcal{J}| \eta_t)}{\partial \eta} \right] - \left[\frac{\partial \tilde{F}}{\partial \xi} + \frac{\partial \tilde{G}}{\partial \eta} \right] \right\}. \quad (8)$$

Equation 8 has a compact form on the computational domain. It offers great ease in handling moving and deformable physical domain as well as parallel computation.

1.2 Time marching scheme

All preliminary computations in this abstract utilize a fourth-order accurate, strong-stability-preserving five-stage Runge-Kutta scheme [6].

1.3 Parallel Capability

The code is MPI parallelized and can run on an arbitrary number of cores. For this case study, the code was run on 8 processors. The following shows the spacial partitioning:

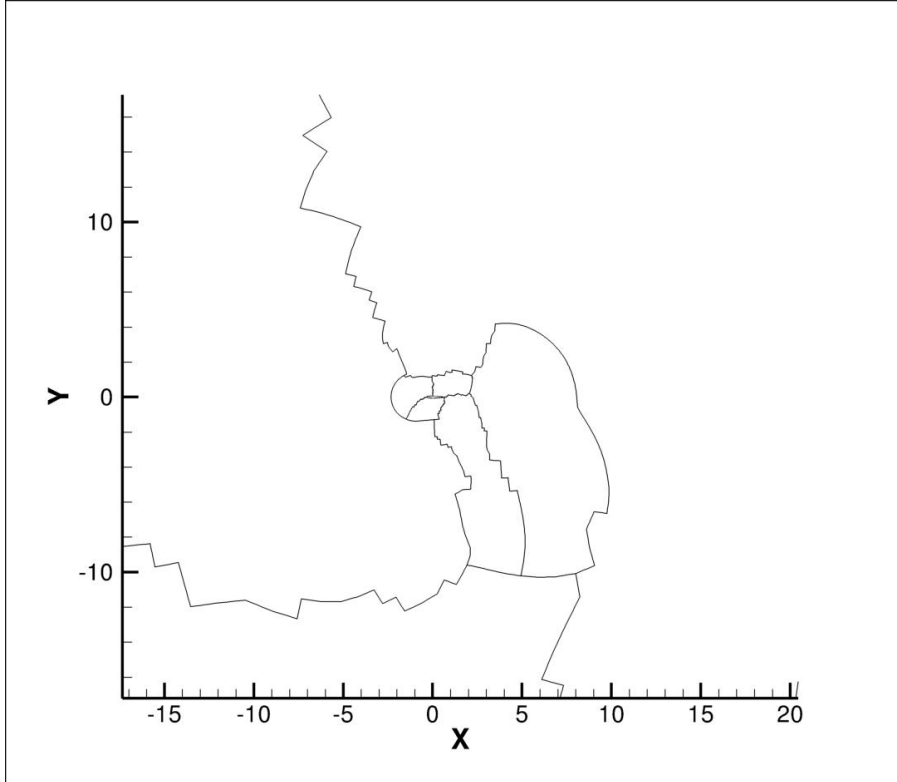


Figure 2: Partition zones for the 8 processors

1.4 Post-Processing

The post-processing for this case includes computation of the total work W and the vertical impulse I from that the fluid exerts on the airfoil, these two quantities are defined as below:

$$W = \int_0^1 f_y(t) \dot{h}(t) dt + \int_0^1 T_z(t) \dot{\theta}(t) dt \quad (9)$$

$$I = \int_0^1 f_y(t) dt, \quad (10)$$

where f_y is the vertical force, $h(t)$ is the vertical displacement, T_z is the torque about the origin, and $\dot{\theta}(t)$ is the pitching angle rate of change in radians per second.

2 Case summary

Case C2.3 is investigated in this report. In this case, an initially stationary airfoil starts pitching and heaving after the surrounding flow reached a steady state. The pitching and heaving last for one period, and we are interested in the total work and the vertical impulse that the fluid exerts on the airfoil. Four separate sub-cases were run to establish the effects of changing the SD order and Reynolds number:

- 3rd order Spectral Difference, $Re = 1,000$

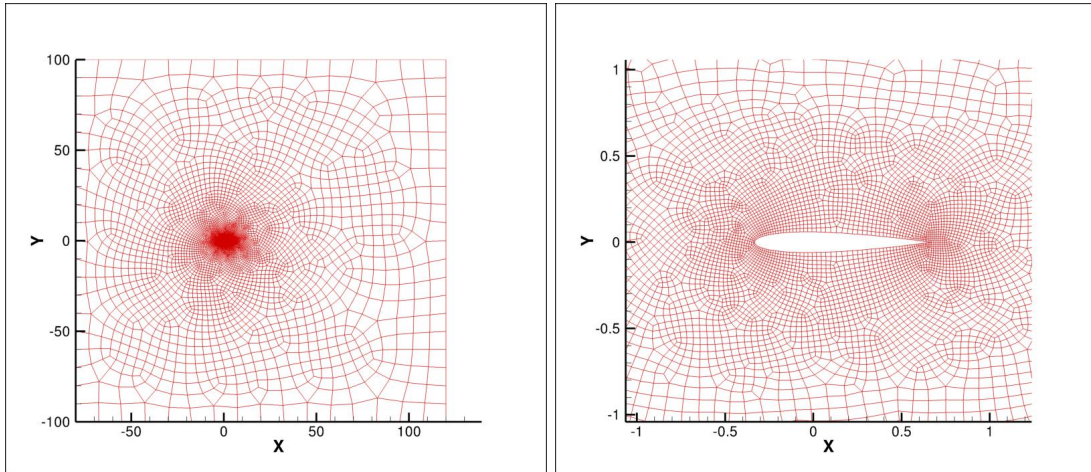
- 3rd order Spectral Difference, $Re = 5,000$
- 5th order Spectral Difference, $Re = 1,000$
- 5th order Spectral Difference, $Re = 5,000$

The SD method is used for the spatial discretization and an explicit five-stage Runge- Kutta scheme is used for the temporal. The time step is set to 5×10^{-5} in all four sub-cases.

The machine used for this test case was a multicore Intel Xeon X5680. Eight of these cores were used for all calculations. For the first 1,000 iterations of the pitching/heaving calculation at a Reynolds number of 5,000 and $N = 5$, the computation time was 237.9 seconds per core. At $N = 3$, this computation time was reduced to 86.05 seconds per core.

3 Meshes

For all sub-cases, the grid space was 200x200 chord lengths with the center of the airfoil located at (0,0). The unstructured grid of quadrilateral cells is shown in Fig. 3 (a). The mesh has 12,670 cells in all. It employs 60 cells along either top or bottom half surface of the NACA0012 airfoil.



(a) Global view of the computational mesh.

(b) Close view of the computational mesh.

Figure 3: Mesh

The inflow boundary is 80 chord lengths away from the airfoil center. The top and bottom boundaries are 100 chord lengths from the center, where the inviscid wall boundary condition is adopted. The outflow flow boundary is located 120 chord lengths away from the airfoil center.

The curved surfaces of the airfoil are handled using a cubic spline fitting. Subsequently, the elements adjacent to the surfaces are mapped to a standard square element with 20 nodal points via a cubic-order mapping.

During the pitching and heaving motion of the airfoil, the grid is deformed by using a blending function. The exact region of the grid that deforms is an annulus with an internal radius of 5 chord lengths and an external radius of 27 chord lengths.

4 Results

The lift and drag forces of airfoil are normalized using $\rho u_\infty^2 C$ where C is the chord of the the airfoil which is unity in this case.

The SD code was specifically modified for this case study to track the work for these test cases. The vertical work is calculated by adding a summation of all of the viscous and pressure-based vertical forces at all the airfoil solution points at each iteration. The vertical work is found using

$$ywork(t) = ywork(t - 1) + \dot{h}(t) \cdot \Delta t \cdot cl_{tot} \cdot \frac{1}{2} \rho_{\infty} \cdot u_{\infty}^2, \quad (11)$$

where $\dot{h}(t)$ is the rate of change of the height of the center of the airfoil, Δt is the time step, and cl_{tot} is the total lift coefficient.

The torsional work is similarly integrated at each solution point by calculating the viscous and pressure-based moments about the origin by using

$$Tqwork(t) = \sum_{i=1}^n [Tqwork(t - 1) + (\Delta x \cdot F_y + \Delta Y \cdot F_x) \cdot \dot{\theta}(t)]^n, \quad (12)$$

where ΔX is the orthogonal distance in the x direction from the current solution point to the origin, F_y is vertical component of the viscous and pressure-based forces, ΔY is the orthogonal distance in the y direction from the current solution point to the origin, F_x is horizontal component of the viscous and pressure-based forces, and $\dot{\theta}$ is the time rate of change of the angle of the airfoil.

The vertical impulse is calculated as shown in Equation 10 in post-processing in order to reduce the iterative computations.

4.1 Case N=3, Re = 1000

Using a 3rd Order SD method and a Reynolds Number of 1,000, the airfoil followed the prescribed pitching and heaving motion after steady-state was achieved. The following Mach contour plots depict the flow fields at $t = 0$ and $t = 1$.

Shown below are the mach number contour plots for $t=0$ and $t=1$.

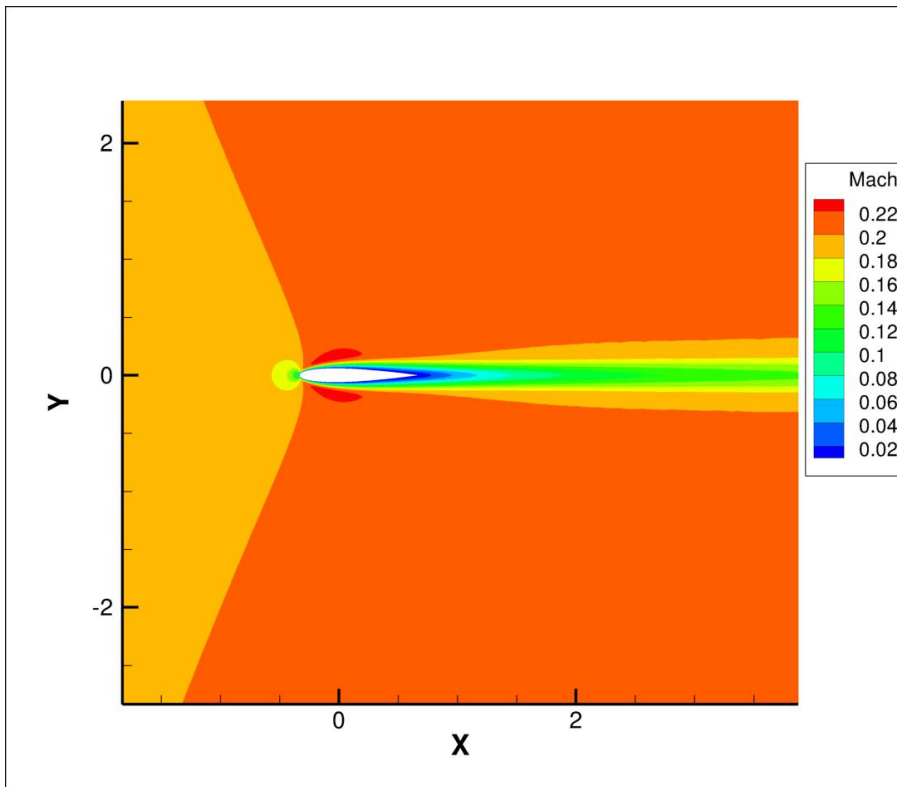


Figure 4: Mach number contour plot at $t=0$

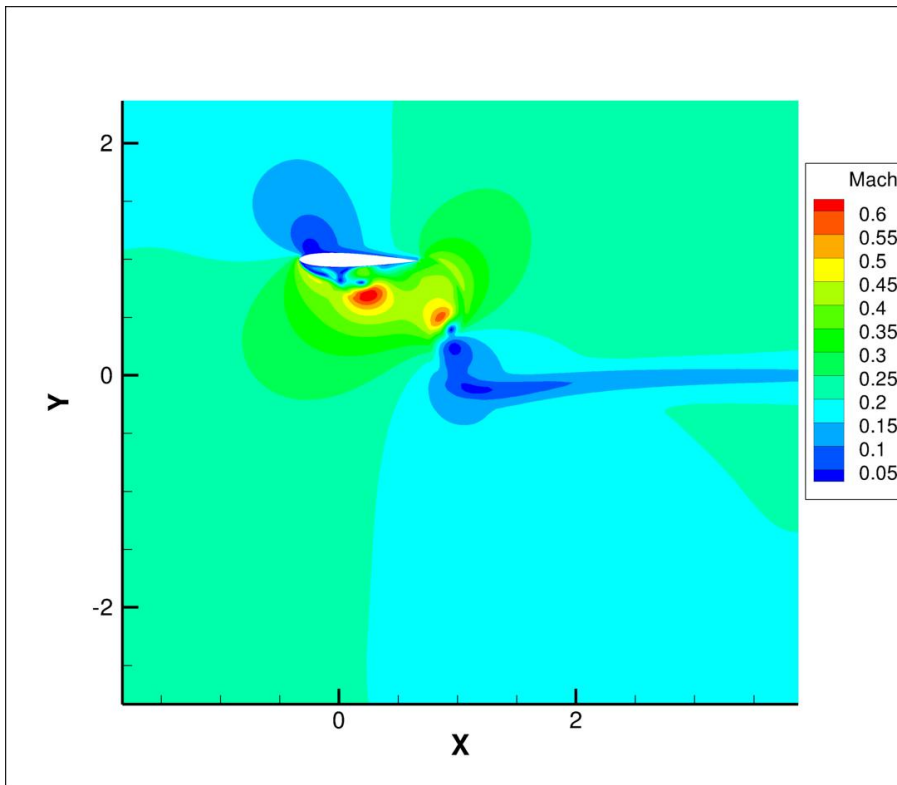


Figure 5: Mach number contour plot at $t=1$

Using the work and impulse equations as shown, the following results were achieved for this particular sub-case:

Vertical Work	Torsional Work	Total Work	Vertical Impulse
-2.6267937385	-0.9057869362	-3.5325806747	-2.1514975345

4.2 Case N=3, Re = 5000

Using a 3rd Order SD method and a Reynolds Number of 5,000, the airfoil followed the prescribed pitching and heaving motion after steady-state was achieved. The following Mach contour plots depict the flow fields at $t = 0$ and $t = 1$.

Shown below are the mach number contour plots for $t=0$ and $t=1$.

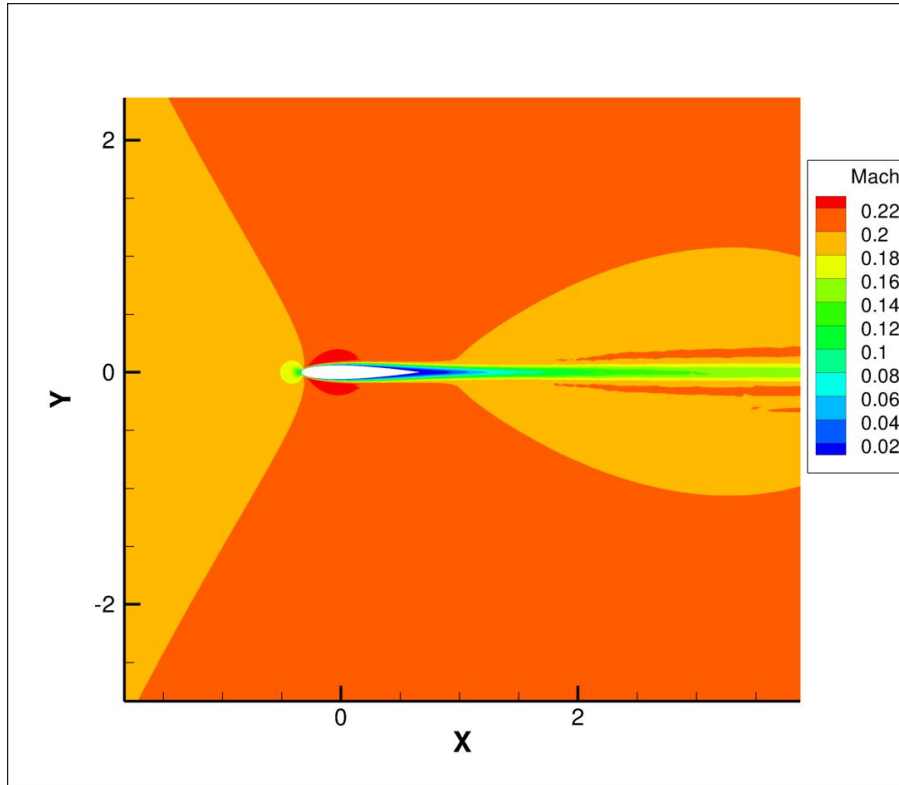


Figure 6: Mach number contour plot at $t=0$

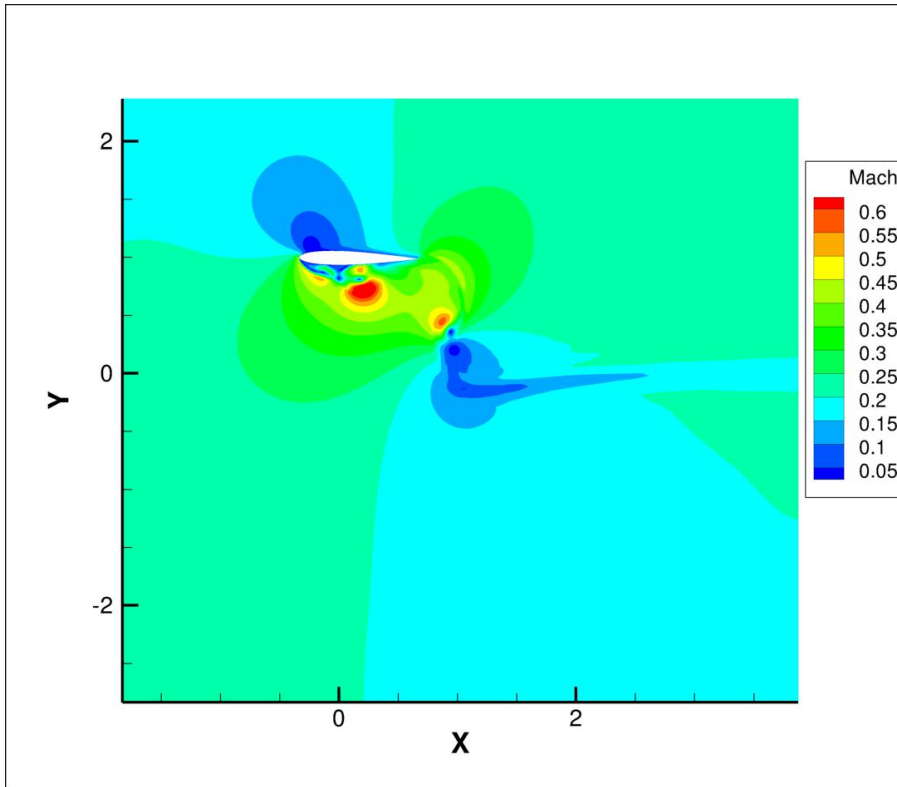


Figure 7: Mach number contour plot at $t=1$

Using the work and impulse equations as shown, the following results were achieved for this particular sub-case:

Vertical Work	Torsional Work	Total Work	Vertical Impulse
-2.6568564138	-1.0273264205	-3.6841828343	-2.2056563772

4.3 Case $N=5$, $Re = 1000$

Using a 5th Order SD method and a Reynolds Number of 1,000, the airfoil followed the prescribed pitching and heaving motion after steady-state was achieved. The following Mach contour plots depict the flow fields at $t = 0$ and $t = 1$.

Shown below are the mach number contour plots for $t=0$ and $t=1$.

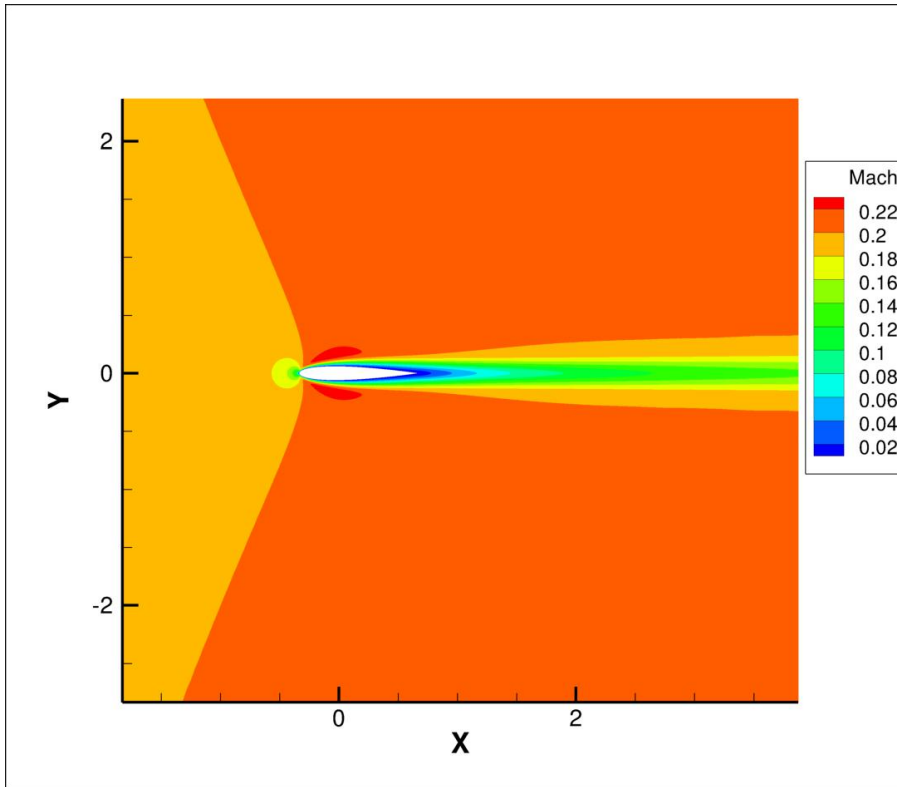


Figure 8: Mach number contour plot at $t=0$

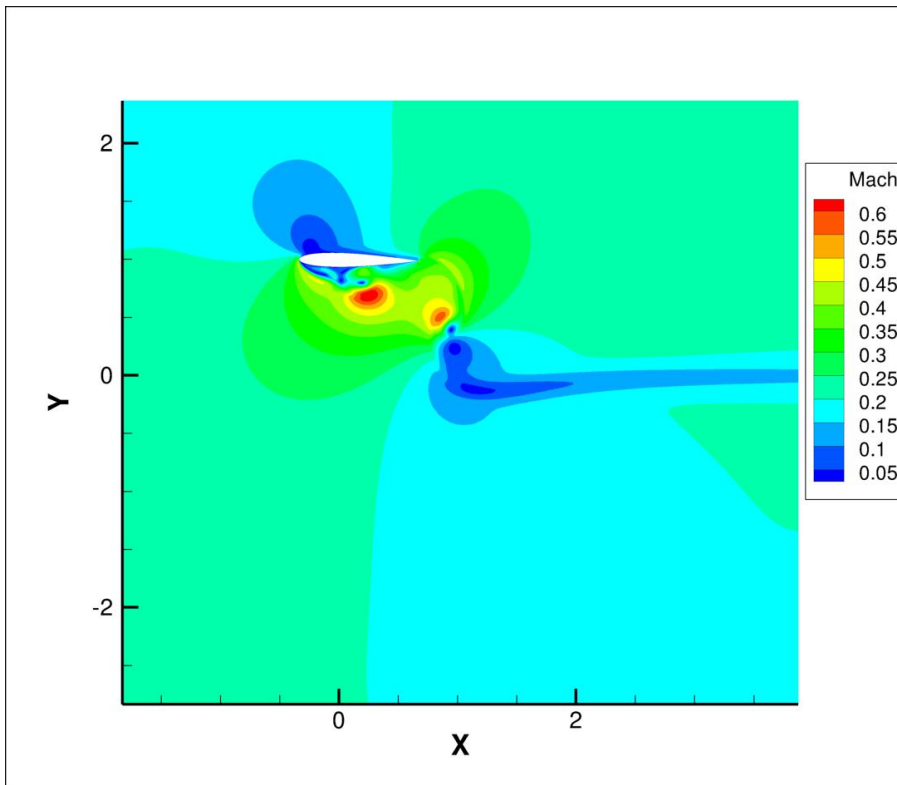


Figure 9: Mach number contour plot at $t=1$

Using the work and impulse equations as shown, the following results were achieved for this particular sub-case:

Vertical Work	Torsional Work	Total Work	Vertical Impulse
-2.6265443136	-0.9069343116	-3.5334786252	-2.1476921744

4.4 Case N=5, Re = 5000

Using a 5th Order SD method and a Reynolds Number of 5,000, the airfoil followed the prescribed pitching and heaving motion after steady-state was achieved. The following Mach contour plots depict the flow fields at $t = 0$ and $t = 1$.

Shown below are the mach number contour plots for $t=0$ and $t=1$.

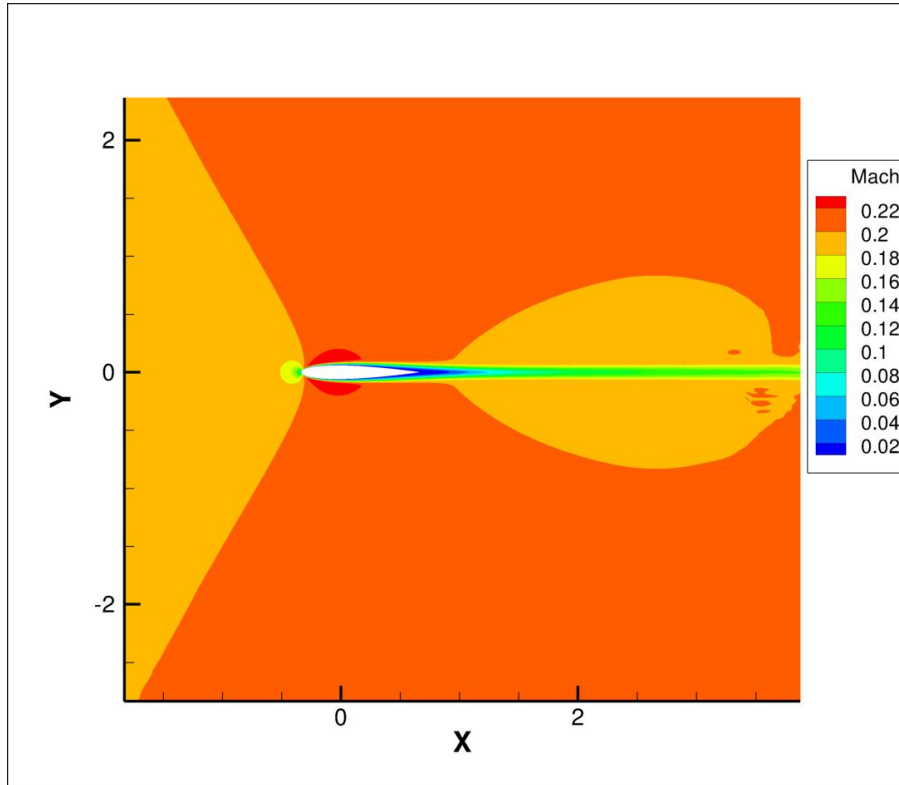


Figure 10: Mach number contour plot at $t=0$

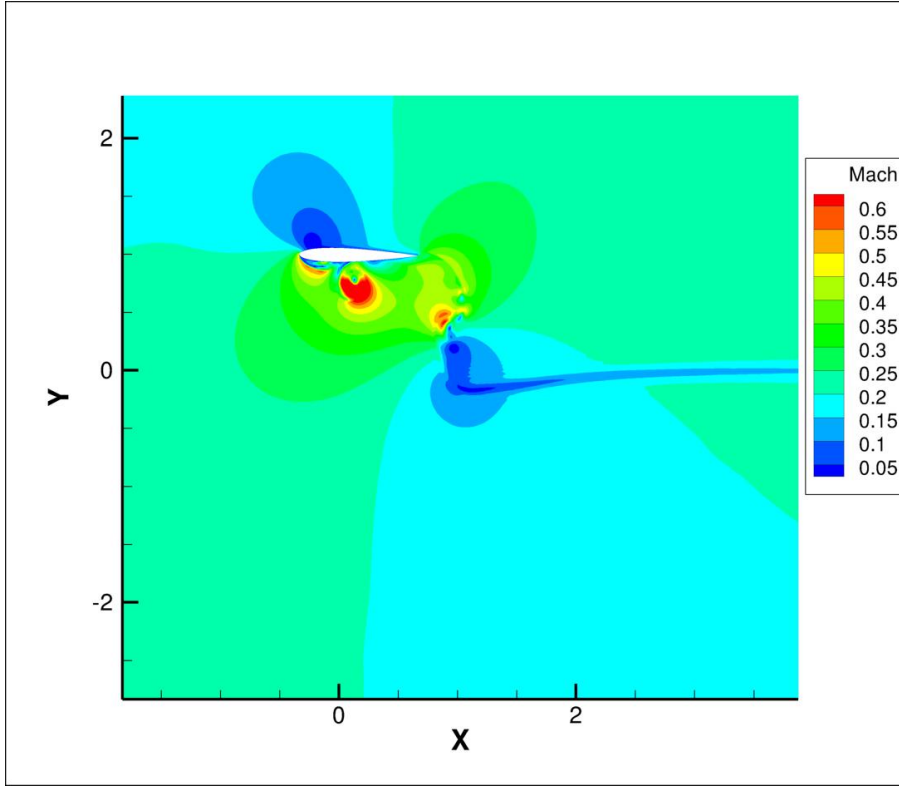


Figure 11: Mach number contour plot at $t=1$

Using the work and impulse equations as shown, the following results were achieved for this particular sub-case:

Vertical Work	Torsional Work	Total Work	Vertical Impulse
-2.716644523	-0.9956179771	-3.7122625001	-2.2001305479

4.5 Conclusion

The results presented above are tabulated below:

Reynolds Number	Order	Total Work	Vertical Impulse
1,000	3	-3.5325806747	-2.1514975345
1,000	5	-3.5334786252	-2.1476921744
5,000	3	-3.6841828343	-2.2056563772
5,000	5	-3.7122625001	-2.2001305479

From these results, it can be seen that increasing the order from $N = 3$ to $N = 5$ produces only small changes in the calculated variables while increasing the computation time by a factor of 2.8. At $Re = 1,000$ increasing the order from $N = 3$ to $N = 5$ changed the calculated vertical impulse by -0.1769% and the total work by 0.0254%. At $Re = 5,000$ increasing the order from $N = 3$ to $N = 5$ changed the calculated vertical impulse by -0.2505% and the total work by 0.762%.

For reference, the lift and drag coefficients from the dynamic tests are also presented below.

From these figures, it can be seen that the results from the 3rd and fifth order calculations show similar results.

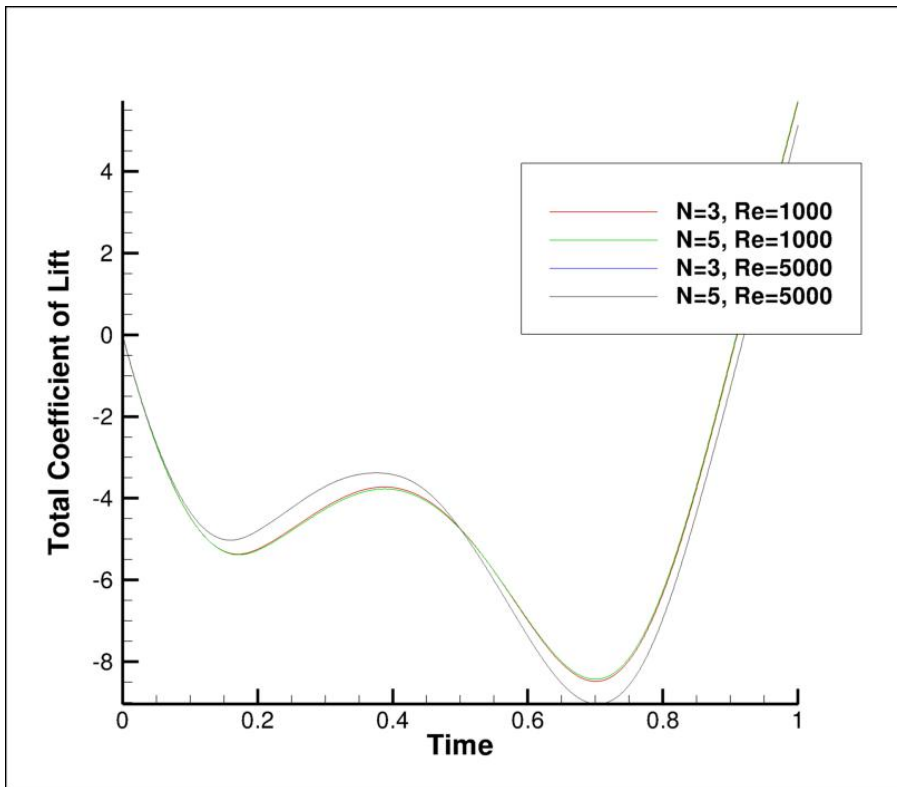


Figure 12: Lift Coefficients for all sub-cases

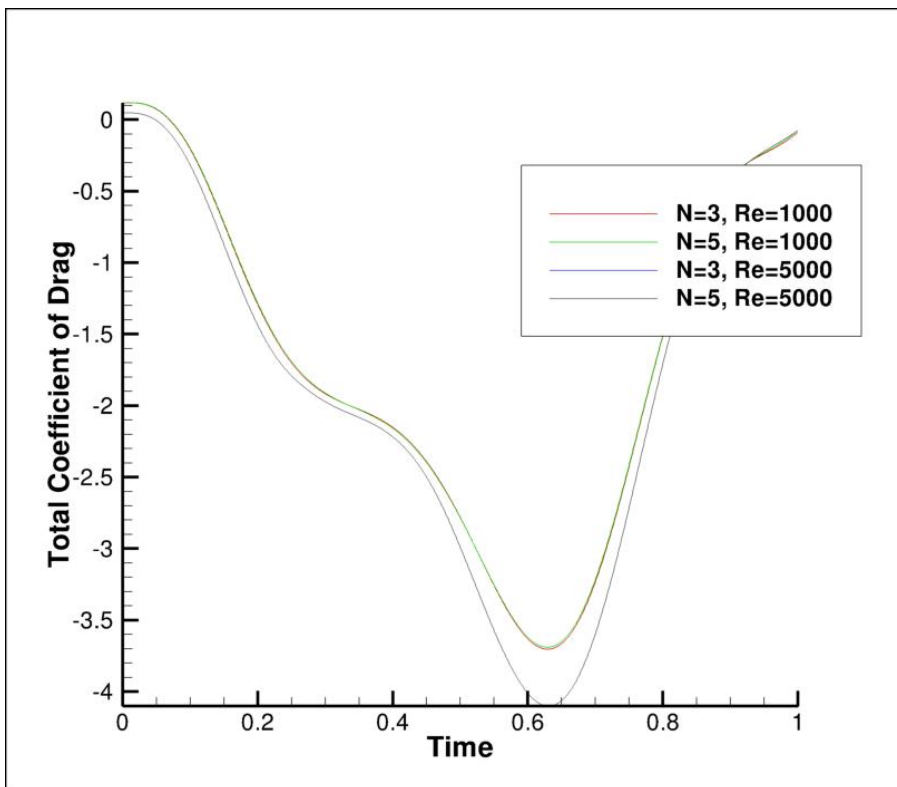


Figure 13: Drag Coefficients for all sub-cases

References

- [1] C. Liang, K. Ou, S. Premasuthan, A. Jameson, and Z. J. Wang. High-order accurate simulations of unsteady flow past plunging and pitching airfoils. *Computers and Fluids*,

40:236–248, 2011.

- [2] C. Liang, A. Jameson, and Z. J. Wang. Spectral difference method for two-dimensional compressible flow on unstructured grids with mixed elements. *Journal of Computational Physics*, 228:2847–2858, 2009.
- [3] M. L. Yu, Z. J. Wang, and H. Hu. A high-order spectral difference method for unstructured dynamic grids. *Computers and Fluids*, 48(1):84 – 97, 2011.
- [4] K. Van den Abeele, C. Lacor, and Z. J. Wang. On the stability and accuracy of the spectral difference method. *J. of Scientific Computing*, 37:162–188, 2008.
- [5] H.T. Huynh. A flux reconstruction approach to high-order schemes including discontinuous Galerkin methods. *AIAA Paper*, AIAA-2007-4079, 2007.
- [6] R. J. Spiteri and S. J. Ruuth. A new class of optimal high-order strong-stability-preserving time discretization methods. *SIAM J. Numer. Anal.*, 40:469–491, 2002.